Stem Cell Reports
Article

ISSCR

OPEN ACCESS

Deregulation of Neuro-Developmental Genes and Primary Cilium Cytoskeleton Anomalies in iPSC Retinal Sheets from Human Syndromic Ciliopathies

Andrea Barabino,[1] Anthony Flamier,[1,6] Roy Hanna,[1] Elise Héon,[2] Benjamin S. Freedman,[3,*] and Gilbert Bernier[1,4,5,7,*]

[1]Stem Cell and Developmental Biology Laboratory, Hôpital Maisonneuve-Rosemont, 5415 Boul. Assomption, Montreal, QC H1T 2M4, Canada
[2]Hospital for Sick Children, Department of Ophthalmology and Vision Sciences, Program of Genetics and Genome Biology, 555 University av., Toronto, ON M5G 1X8, Canada
[3]Department of Medicine, Division of Nephrology, Kidney Research Institute, and Institute of Stem Cell and Regenerative Medicine, and Department of Pathology, University of Washington School of Medicine, Seattle, WA 98109, USA
[4]Department of Neurosciences, University of Montreal, Montreal, QC H3C 3J7, Canada
[5]Department of Ophthalmology, University of Montreal, Montreal, QC H3C 3J7, Canada
[6]Present address: Whitehead Institute for Biomedical Research, Massachusetts Institute of Technology (MIT), 455 Main Street, Cambridge, MA 02142, USA
[7]Lead Contact
*Correspondence: benof@uw.edu (B.S.F.), gbernier.hmr@ssss.gouv.qc.ca (G.B.)
https://doi.org/10.1016/j.stemcr.2020.02.005

SUMMARY

Ciliopathies are heterogeneous genetic diseases affecting primary cilium structure and function. Meckel-Gruber (MKS) and Bardet-Biedl (BBS) syndromes are severe ciliopathies characterized by skeletal and neurodevelopment anomalies, including polydactyly, cognitive impairment, and retinal degeneration. We describe the generation and molecular characterization of human induced pluripotent stem cell (iPSC)-derived retinal sheets (RSs) from controls, and MKS (TMEM67) and BBS (BBS10) cases. MKS and BBS RSs displayed significant common alterations in the expression of hundreds of developmental genes and members of the WNT and BMP pathways. Induction of crystallin molecular chaperones was prominent in MKS and BBS RSs suggesting a stress response to misfolded proteins. Unique to MKS photoreceptors was the presence of supernumerary centrioles and cilia, and aggregation of ciliary proteins. Unique to BBS photoreceptors was the accumulation of DNA damage and activation of the mitotic spindle checkpoint. This study reveals how combining cell reprogramming, organogenesis, and next-generation sequencing enables the elucidation of mechanisms involved in human ciliopathies.

INTRODUCTION

Primary cilia are typically non-motile cytoplasmic extensions of a microtubule-based structure that projects from the cell surface and are indispensable for normal developmental and physiological functions (Nonaka et al., 1998; Satir et al., 2007). The ciliary axoneme develops from and is anchored to a specialized centriole called the basal body (BB) that acts as a microtubule organizing center. The BB is a symmetric radial arrangement of nine triplet microtubules from which the outer doublet of microtubules of the axoneme extends. Syndromic and non-syndromic ciliopathies represent a group of heterogeneous genetic diseases caused by mutations affecting the structure and function of the primary cilium. Phenotypic and genetic heterogeneity is frequently observed in these diseases. The relationship between cilia genes and ciliopathies is far more complex than that described by classical Mendelian genetics and has recently been the focus of numerous reviews (Loncarek and Bettencourt-Dias, 2018; Vertii et al., 2015; Wheway et al., 2018).

Meckel-Gruber syndrome (MKS) and Bardet-Biedl syndrome (BBS) are rare developmental diseases characterized by multiple developmental anomalies, including retinal degeneration, digits and genito-urinary defects, as well as cognitive impairment (Leitch et al., 2008; Álvarez-Satta et al., 2017). Although MKS is fatal at birth, BBS is one of the most severe ciliopathies that is compatible with life. MKS is a lethal autosomal recessive ciliopathy, also presenting polycystic kidneys and severe eye/brain malformations, with over 13 disease-associated genes (Delous et al., 2007; Kyttälä et al., 2006; Smith et al., 2006; OMIM, 2019a). In contrast, BBS is a viable disorder associated with obesity and retinal degeneration (Leitch et al., 2008; Álvarez-Satta et al., 2017) and with variants identified in over 22 genes, with *BBS10* representing the most commonly mutated gene (Nishimura et al., 2004; OMIM, 2019b). MKS and BBS were in principle considered as two distinct clinical entities. However, the identification of hypomorphic mutations in *MKS1* and *TMEM67* in some BBS patients introduced the concept that BBS may represent a milder form of MKS (Leitch et al., 2008). The MKS3 protein (encoded by *TMEM67*) is apparently not an integral part of the MKS complex, but more likely to interact with it (Leitch et al., 2008; Smith et al., 2006). MSK3 localizes to the transition zone at the base of the primary cilium, and

This is an open access article under the CC BY-NC-ND license (http://creativecommons.org/licenses/by-nc-nd/4.0/).

to the plasma membrane in ciliated cells (Reiter et al., 2012). MKS3 has been associated with centrosome migration to the apical cell surface during early ciliogenesis and with the regulation of centrosome organization (Adams et al., 2012; Gupta et al., 2015). The BB derives from the mother centriole, which distinguishes it from the daughter centriole by the presence of appendages on its distal end, allowing the formation of the primary cilium (Chang et al., 2003). Centriolin (also known as CEP110 or CNTRL) is associated with the mother centriole (Ou et al., 2002). Mutations in *CNTRL* can cause ciliopathies as atrioventricular septal defect (Burnicka-Turek et al., 2016). Although many BBS-associated proteins are an integral part of the BBSome complex, BBS10 most likely interacts with the BBSome and shows sequence similarities with chaperones (Stoetzel et al., 2006).

The vast majority of genes causing retinal degeneration involves a defect in a ciliary protein (RetNet). Molecular and cellular insights found in this work are potentially relevant to other ciliopathies and non-syndromic retinal disorders. Degeneration of photoreceptors (PRs) is often part of syndromic ciliopathies (Adams et al., 2007; Novarino et al., 2011). Retinal degeneration varies depending on the type of PRs that are primarily affected. Rods respond to dim light and are important for night and peripheral vision. Cones respond to intense light and are required for color, daylight, and high-resolution central vision (Aboshiha et al., 2016). The inner segment (IS) and outer segment (OS) of PRs, which respectively represent the metabolic factory and the structure where phototransduction takes place, are connected by the connecting cilium (CC), which is a modified intracellular version of the primary cilia (Young, 1968). The proteins synthesized in the IS are transported to the base of the CC in post-Golgi vesicles in an area also called the transition zone, where they are associated with molecular transport complexes that allow bidirectional movement along the axoneme, called intraflagellar transport (IFT) (Khanna, 2015; Pazour et al., 2002). The IFT family and other BB-associated proteins, if mutated, may cause mislocalization and accumulation of OS proteins in the IS, causing PR degeneration (Marszalek et al., 2000; Pazour et al., 2002). The RPGR, RP1, and RP2 proteins mostly localize at the BB of the CC, and mutations in these are a leading cause of retinitis pigmentosa (Breuer et al., 2002).

Although valuable, animal models have shown limitations in modeling retinal ciliopathies, with patient-derived induced pluripotent stem cells (iPSCs) representing a new opportunity for modeling human diseases (Grandy et al., 2019). Structures like the macula, responsible for high-resolution central vision, are not present in most commonly used animal models. Moreover, the PR's ultrastructure between mice and humans differs at the transition zone, an area adjacent to the CC. Here, we found structures called calyceal processes which are present in human but not in mice. Likewise, the USH1G/1C proteins, which are mutated in Usher syndrome, localize to the CC of human PRs but have no equivalent in rodents (Sahly et al., 2012). We report here on the generation of iPSCs from MKS and BBS cases and on their differentiation into retinal sheets (RSs) containing cone PRs (Zhou et al., 2015). We found that RSs from MKS and BBS cases displayed common alterations in hundreds of developmental genes, including homeobox and *HOX* genes, as well as genes of the WNT, NOTCH, and BMP signaling pathways. MKS PRs showed supernumerary cilia and centrioles and mislocalization of ciliary proteins. BBS PRs presented mitotic spindle checkpoint activation, DNA damage, and genomic instability. Both MKS and BBS PRs accumulated chaperones of the crystallin gene family, suggesting a cellular response to misfolded proteins and/or proteasome dysfunction. This study brings new molecular and cell biological information on the neurodevelopmental and retinal degeneration anomalies associated with human syndromic ciliopathies.

RESULTS

Generation and Characterization of iPSC-Derived RSs

We have generated iPSCs from skin fibroblasts of three healthy volunteers ($Ctrl^{01}$, $Ctrl^{02}$, and $Ctrl^{03}$), two unrelated MKS cases (MKS^{01} and MKS^{02}), and two unrelated BBS cases (BBS^{01} and BBS^{02}). The iPSCs expressed pluripotency markers, were able to form teratomas and could be differentiated into embryoid bodies containing retinal pigment epithelium (RPE) upon exposure to nicotinamide (Figures S1A–S1D). The presence of an external cilium was also observed in iPSCs using scanning electron microscopy (Figure S1B). By whole-genome sequencing (WGS) of the iPSC lines, we found that both BBS cases carried different mutations in *BBS10*, with a homozygous mutation causing a frameshift stop in the first case (c.271dup), and a compound heterozygous mutation in the second case (c.909_912del; c.687del) (Figures S1E–S1G). The MKS^{01} case carried compound heterozygous permutations at the *TMEM67* locus (c.233G > A; c.1046T > C) predicted to be pathogenic (Figures S1E–S1G). We could not, however, confirm the disease-causing mutation in the MKS^{02} case.

Control, $BBS^{01/02}$, and $MKS^{01/02}$ iPSCs were differentiated for 60 days *in vitro* (DIV) into RSs using the same methodology as for human embryonic stem cells (hESCs) (Zhou et al., 2015). Control RSs were analyzed by confocal immunofluorescence. 3D reconstruction imaging revealed the generation of a polarized, multi-layered tissue expressing OS (peanut agglutinin [PNA] and S-opsin), CC (acetylated

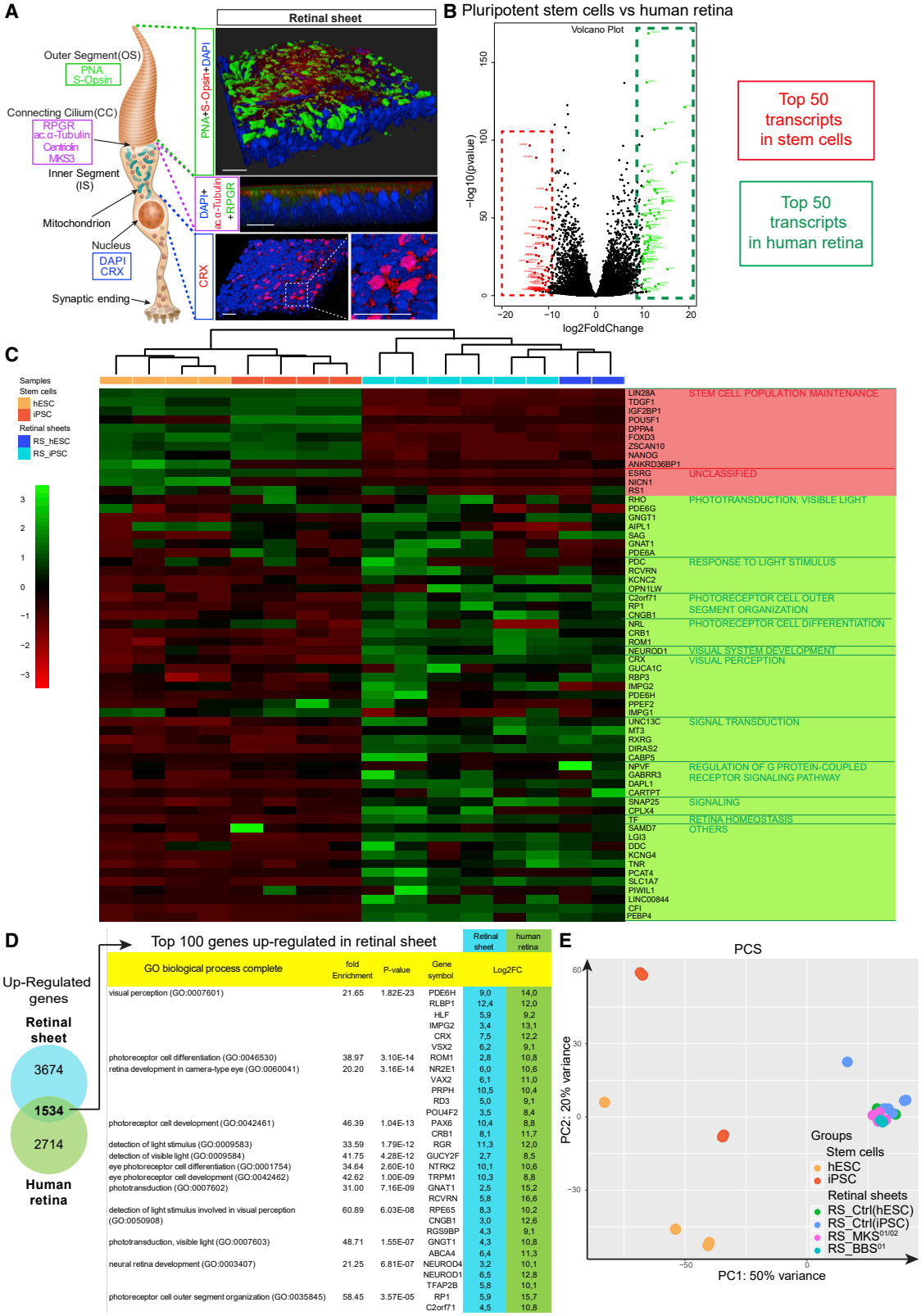

GO biological process complete	fold Enrichment	P-value	Gene symbol	Log2FC Retinal sheet	Log2FC human retina
visual perception (GO:0007601)	21.65	1.82E-23	PDE6H	9,0	14,0
			RLBP1	12,4	12,0
			HLF	5,9	9,2
			IMPG2	3,4	13,1
			CRX	7,5	12,2
			VSX2	6,2	9,1
photoreceptor cell differentiation (GO:0046530)	38.97	3.10E-14	ROM1	2,8	10,8
retina development in camera-type eye (GO:0060041)	20.20	3.16E-14	NR2E1	6,0	10,6
			VAX2	6,1	11,0
			PRPH	10,5	10,4
			RD3	5,0	9,1
			POU4F2	3,5	8,4
photoreceptor cell development (GO:0042461)	46.39	1.04E-13	PAX6	10,4	8,8
			CRB1	8,1	11,7
detection of light stimulus (GO:0009583)	33.59	1.79E-12	RGR	11,3	12,0
detection of visible light (GO:0009584)	41.75	4.28E-12	GUCY2F	2,7	8,5
eye photoreceptor cell differentiation (GO:0001754)	34.64	2.60E-10	NTRK2	10,1	10,6
eye photoreceptor cell development (GO:0042462)	42.62	1.00E-09	TRPM1	10,3	8,8
phototransduction (GO:0007602)	31.00	7.16E-09	GNAT1	2,5	15,2
			RCVRN	5,8	16,6
detection of light stimulus involved in visual perception (GO:0050908)	60.89	6.03E-08	RPE65	8,3	10,2
			CNGB1	3,0	12,6
			RGS9BP	4,3	9,1
phototransduction, visible light (GO:0007603)	48.71	1.55E-07	GNGT1	4,3	10,8
			ABCA4	6,4	11,3
neural retina development (GO:0003407)	21.25	6.81E-07	NEUROD4	3,2	10,1
			NEUROD1	6,5	12,8
			TFAP2B	5,8	10,1
photoreceptor cell outer segment organization (GO:0035845)	58.45	3.57E-05	RP1	5,9	15,7
			C2orf71	4,5	10,8

(legend on next page)

α-tubulin and RPGR), and nuclear pan-PR (CRX) markers (Figure 1A), suggesting efficient differentiation into RSs. Using RNA sequencing (RNA-seq), we compared the transcriptome of control RSs with that of the Human Retinal Development Atlas (Hoshino et al., 2017), and found that RSs clustered with human embryonic retinas at days 80 and 94. RNA-seq data from control RSs were also compared with the top 50 most upregulated transcripts in adult human retina and the top 50 iPSC-specific transcripts (Li et al., 2014) (Figure 1B). Retinal and PR-specific transcripts, including *NR2E1*, *GRK1*, *CRX*, *PDE6H*, *RXRG*, *ROM1*, *CRB1*, *RPE65*, *PRPH*, *RP1*, *RCVRN*, *ABCA4*, and *GNAT1*, were significantly enriched in RSs. In contrast, iPSC-specific transcripts were lost in RSs, suggesting efficient cellular differentiation (Figure 1C). Despite the presence of rod-specific transcripts in RSs, we failed to detect rhodopsin protein expression using immunoblot or immunofluorescence.

When comparing the entire gene dataset of undifferentiated iPSCs with that of adult human retinas and RSs, we found that 1,534 genes were commonly upregulated in human retinas and RSs. Gene ontology analysis of the top 100 genes revealed that these were primarily implicated in the detection of light stimuli, PR OS organization, PR development and visual perception (Figure 1D). We also performed a principal-component analysis of RSs and iPSC/hESC lines. Although iPSCs and hESCs were generally scattered, RSs from all samples were grouped together, suggesting cellular differentiation toward a common lineage (Figure 1E). We next used immunoblot to test if RSs expressed PR-specific proteins. We found that $Ctrl^{01/02/03}$, $MKS^{01/02}$, and $BBS^{01/02}$ RSs were all expressing CRX (expressed in PR and in a subset of bipolar neurons) and S-opsin (expressed exclusively in cone PRs) (Figure 2A). Taken as a whole, these results suggested robust differentiation of iPSC lines into RSs.

Deregulation of Neurodevelopmental Genes in MKS and BBS RSs

We compared RNA-seq data from $Ctrl^{01/02}$, $MKS^{01/02}$, and BBS^{01} RSs and found thousands of genes commonly dysregulated in ciliopathies (Figures 2B and 2C). A total of 1,597 genes were dysregulated in both BBS^{01} and $MKS^{01/02}$ samples when compared with controls (661 upregulated, 936 downregulated) (Figures 2D and 3A). Among the 661 commonly upregulated genes, most were related to neural/retinal development (*DLX1*, *VSX1*, and *SIX6*), differentiation (*NEUROD4* and *ASCL1/MASH1*), and function (*SLC32A1* and *NTRK1*), while others were associated with ganglion and amacrine cell fate, suggesting premature and/or increased neurogenesis and perturbed retinal cell fate specification in ciliopathies (Figures 2E–2G and S2A–S2D). Different homeobox genes including members of the HOX family were also upregulated in both BBS^{01} and $MKS^{01/02}$ RSs (Figure S2A). Defective NOTCH and/or WNT signaling is frequently associated with premature neurogenesis and/or cell-cycle exit of neural progenitors (Ma et al., 2019; Navarro Quiroz et al., 2018). Hence, we found altered expression of genes of the WNT and NOTCH signaling pathways in both MKS and BBS RSs (Figures S2B and S2C). Further analyses suggested major deregulation of WNT signaling in ciliopathies toward the canonical pathway at the expense of the non-canonical one, which is known to play a role in planar cell polarity and cilia formation (Figure S2B) (May-Simera and Kelley, 2012).

Alterations of Genes Involved in Development, Morphogenesis, and Cilia Formation

When analyzing genes commonly downregulated in BBS^{01} and $MKS^{01/02}$ RSs, we found significant alteration of genes involved in development (112 genes) and/or morphogenesis (138 genes) (Figures 3A–3C). We next grouped these

Figure 1. Generation of iPSC-Derived Retinal Sheets

(A) Representation of a cone PRs (left) and 3D reconstruction of an RS (right) with reference to the main compartments, outer segment (OS), connecting cilium (CC), inner segment (IS), and nucleus. For each compartment are indicated the main markers used in this paper: peanut agglutinin (PNA) and S-opsin for the OS; acetyl-α-tubulin and RPGR for the CC; CRX for the nucleus. Scale bars, 40 μm.

(B) Volcano plot from RNA-seq analyses between human retina (n = 2 independent biological samples) and undifferentiated stem cells (n = 4 iPSCs; n = 4 hESCs, independent cell lines). The red points show the 50 most significantly downregulated genes (stem cell-related genes). The green points show the 50 most significantly upregulated genes (human retina-related genes).

(C) Heatmap showing differential expression for stem cell and human retina-related genes between undifferentiated stem cells lines (n = 4 iPSCs; n = 4 hESCs) and Ctrl RSs (n = 8 from 3 independent iPSC and 1 hESC lines). Hierarchical clustering by Pearson's correlation clearly distinguishes the two groups.

(D) Venn diagrams showing the intersection of significant genes differentially upregulated in control RSs ($Ctrl^{01}$, $Ctrl^{02}$, $Ctrl^{03}$, and hESC-Ctrl) and in human retina. Gene ontology enrichment analysis of the 100 most upregulated genes in RSs compared with undifferentiated iPSCs that are also upregulated in the human retina ($p < 0.05$). For every gene ontology (GO) group, we indicated their fold enrichment, p values, and few representative genes. For every gene are indicated log2FC in Ctrl_RSs (light blue) and in human retina (green).

(E) Principal-component analysis (PCA) between stem cells (iPSCs and ESCs) and RSs from control iPSCs and hESCs, and RS from MKS (n = 4 from 2 patients) and BBS (n = 2 from 1 patient). Notice how all RSs cluster together, while PSCs are more dispersed.

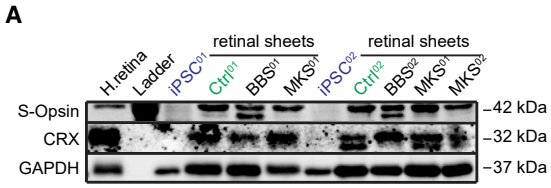

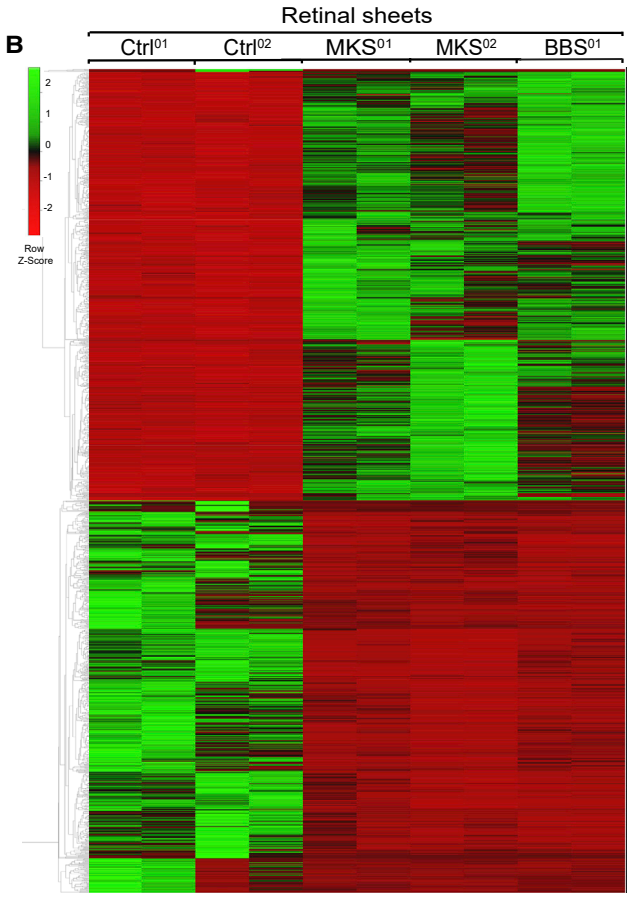

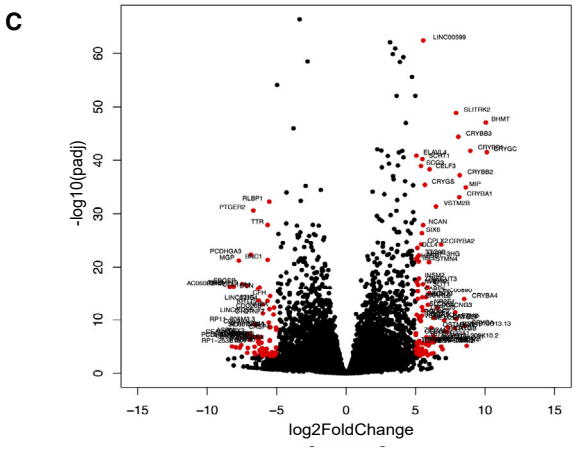

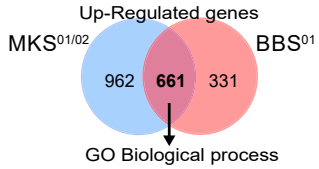

E

Neural retina function, development and morphogenesis	Gene Symbol	Log2FC MKS	Log2FC BBS
visual perception(GO:0007601)	GJA8	6,5	4,7
	GJA3	2,1	2,1
	RGS16	3,0	2,1
	IMPG2	4,6	3,1
	GUCY2D	3,6	3,1
	CHRNB2	4,1	3,5
	ZIC2	2,2	2,4
	MIP	8,4	8,7
	COL2A1	2,3	2,5
	VSX2	4,2	5,2
	RBP3	4,9	4,4
	CACNA1F	3,2	2,8
	PDC	4,6	4,4
	CLRN1	2,7	3,2
	RAX2	5,3	3,9
	NDP	5,3	3,2
	VSX1	5,5	4,6
	CNGA3	4,7	3,8
	RCVRN	4,3	4,3
	KCNJ10	3,8	4,4
phototransduction, visible light (GO:0007603)	AIPL1	3,9	3,3
	PDE6C	3,4	2,3
retinal cone cell development (GO:0046549	RORB	3,5	3,9
	DIO3	3,9	2,2
eye photoreceptor cell development (GO:0042462)	CRB1	3,3	3,6
	PRDM1	4,1	4,5
	TH	3,1	2,8
retina development in camera-type eye (GO:0060041)	GRM6	4,6	3,7
	NR2E1	6,3	4,6
	POU4F2	4,5	5,8
regulation of neural retina development (GO:0061074)	DLL4	4,6	5,8
	PTF1A	4,5	5,7
neural retina development (GO:0003407)	ATOH7	4,6	6,4
	SLC17A7	3,4	3,3
eye development (GO:0001654)	FOXE3	7,2	6,8
	SIX6	5,3	5,8
	SOX2	3,1	2,2
	RBP4	3,5	3,7
	CHRDL1	3,6	2,3
camera-type eye development (GO:0043010)	HES5	4,6	5,6
	PAX2	8,4	3,6
camera-type eye morphogenesis (GO:0048593)	AQP5	2,0	2,2

F

Retinal ganglion cell development	Gene Symbol	Log2FC MKS	Log2FC BBS
retinal ganglion cell axon guidance (GO:0031290)	ISL2	5,3	5,3
	ISL1	5,1	4,6
	SLIT1	6,3	3,4
	POU4F2	4,5	5,8
	NRCAM	3,9	2,7
optic nerve development (GO:0021554)	ATOH7	4,6	6,4
	PAX2	8,4	3,6
	NTRK1	3,4	4,2
	DRGX	3,1	3,6
	POU4F1	4,4	3,2

G

Amacrine cell development	Gene Symbol	Log2FC MKS	Log2FC BBS
amacrine cell differentiation (GO:0035881)	NEUROD4	5,4	4,9
	NEUROD1	4,8	5,3
	FOXN4	3,6	4,4
	PTF1A	4,5	5,7
positive regulation of amacrine cell differentiation (GO:1902871)	DLX1	6,7	4,6
	DLX2	4,9	3,4

(legend on next page)

genes among the most representative clusters and compared them by focusing on genes common to different organs/systems (Figures 3A–3D). We found five developmental genes—*Noggin* (*NOG*), *SIX1*, *BMP4*, *CDH19*, *OSR1*—all involved in kidney, heart, ear, skeletal, circulatory, and retinal development (Ahmed et al., 2012; Wu et al., 2014). Three of them, *NOG*, *SIX1*, and *OSR1*, were also present in most of the morphogenetic groups. Other genes, such as *MSX1*, *TWIST1*, *SIX2*, and *OSR2* were present in some of the morphogenetic and developmental groups (Figure 3B) (Goodnough et al., 2016; Li et al., 2003; Paradowska-Stolarz, 2015). *PITX2* was one of the most downregulated developmental genes in both $MKS^{01/02}$ and BBS^{01} RSs (Figure 3D). Notably, a large number of genes involved in cilium assembly/organization and intraciliary transport were downregulated in MKS and BBS RSs (Figures S3A–S3C) (HUGO, 2019). From these, 21 corresponded to the cilia- and flagella-associated protein gene family (Figure S3B). We also found 962 genes upregulated and 684 genes downregulated only in $MKS^{01/02}$ RSs (Figures S3D–S3H). Among these, many were associated with the development and anterior-posterior pattern specification (Figures S3E and S3H). Several genes of the HOX family were also specifically upregulated only in $MKS^{01/02}$ RSs, in agreement with MKS being the most severe form of syndromic ciliopathy (Figure S3F).

Induction of the Crystallin Molecular Chaperones in MKS and BBS RSs

From the top 10 most upregulated genes common to BBS and MKS RSs, we found that six encoded members of the crystallin gene family (Figures S4A–S4C) (Kamachi et al., 2001). In non-lens tissues, these proteins work as molecular chaperones against protein misfolding. Using immunoblot and immunofluorescence, we observed specific accumulation of CRYBB1, CRYBB2, and CRYBB3 in both the nuclear and cytoplasmic cell compartments of BBS^{01} and MKS^{01} PRs at DIV45 (Figures 4A–4C, S4A, and S4B). Polyubiquitin chains at lysine 48 (polyUb-K48) mark proteins for proteasomal degradation and poly-ubiquitylated proteins frequently accumulate in neurodegenerative diseases (Smith et al., 2015). When compared with control RSs, MKS^{01} and MKS^{02}, but not BBS^{01} RSs, presented increased polyUb-K48 levels, suggesting perturbed proteostasis (Figure 4B). Accumulation of misfolded proteins is frequently associated with neuronal cell death (Tzekov et al., 2011). Accordingly, we observed increased expression of apoptosis and cell death-related genes in $MKS^{01/02}$ and BBS^{01} RSs (Figure S4D). Induction of PR cell death in MKS and BBS RSs was also confirmed using the TUNEL assay and transmission electron microscopy (TEM) (Figures 4D–4I and S4E–S4H). These results suggested a cellular response to misfolded proteins and increased cell death in $MKS^{01/02}$ and BBS^{01} PRs.

MKS PRs Are Characterized by the Presence of Supernumerary Centrioles

We performed cell biological analyses to study the structure of the cilium in MKS and BBS PRs. The centriole forms the basement of the primary cilium, and Centriolin marks the mother centriole and BB (Chang et al., 2003). Using an antibody against Centriolin, we found that, when compared with controls, the number of centrioles per cell was higher in DIV60 $MKS^{01/02}$ PRs, but not in $BBS^{01/02}$ PRs (Figures 5A and 5B). This was confirmed by TEM (Figures 5C and 5D), where cilia also appeared to be shorter in MKS (Figures 5C and 5D). Although the total number of cells tended to be higher in MKS and BBS cultures, the difference was not significant (not shown). Notably, supernumerary centrioles were not observed in undifferentiated MKS^{01} iPSCs (Figures S5A–S5C), suggesting that the defect was cell-type specific.

We did not elucidate the pathogenic mutation in the MKS^{02} case. However, in the MKS^{01} case, the two identified mutations in *TMEM67* were predicted to generate a pathogenic but full-length variant of MKS3 (Figures S1G and

Figure 2. Neurodevelopmental Anomalies in MKS and BBS RSs

(A) Immunoblot on extracts from a human retina (positive ctrl), undifferentiated iPSCs (negative ctrl), and RSs from $Ctrl^{01/02}$, $BBS^{01/02}$, and $MKS^{01/02}$ patients.

(B) Heatmap of gene expression profile for differentially expressed genes between $Ctrl^{01/02}$ ($n = 4$ from 2 independent ctrl cell lines), $MKS^{01/02}$ ($n = 4$ from two independent MKS patients), and BBS^{01} ($n = 2$ from one BBS patient) ($p < 0.0001$: up, log2FC > 2; down, log2FC < −2). Hierarchical clustering by average linkage with Kendall's Tau correlation clearly distinguishes control and patient RSs.

(C) Volcano plot from RNA-seq analyses between $Ctrl^{01/02}$ and all patient RSs. The red points show the most significantly dysregulated genes (log2FC > 5 and adjusted $p < 0.001$).

(D) Venn diagrams showing the intersection of significant genes differentially upregulated in $MKS^{01/02}$ (blue, 1,623 genes) and in BBS^{01} RSs (red, 992 genes) (log2FC > 2; $p < 0.05$).

(E–G) Gene ontology enrichment analyses of common differentially upregulated genes between the two groups (E) Neural retina function, development and morphogenesis, (F) Retinal ganglion cell development, (G) Amacrine cell development. Some of the main GO groups and subgroups are shown with some indicative genes and the respective log2FC in $MKS^{01/02}$ (orange column) and BBS^{01} RSs (green column) ($p < 0.05$).

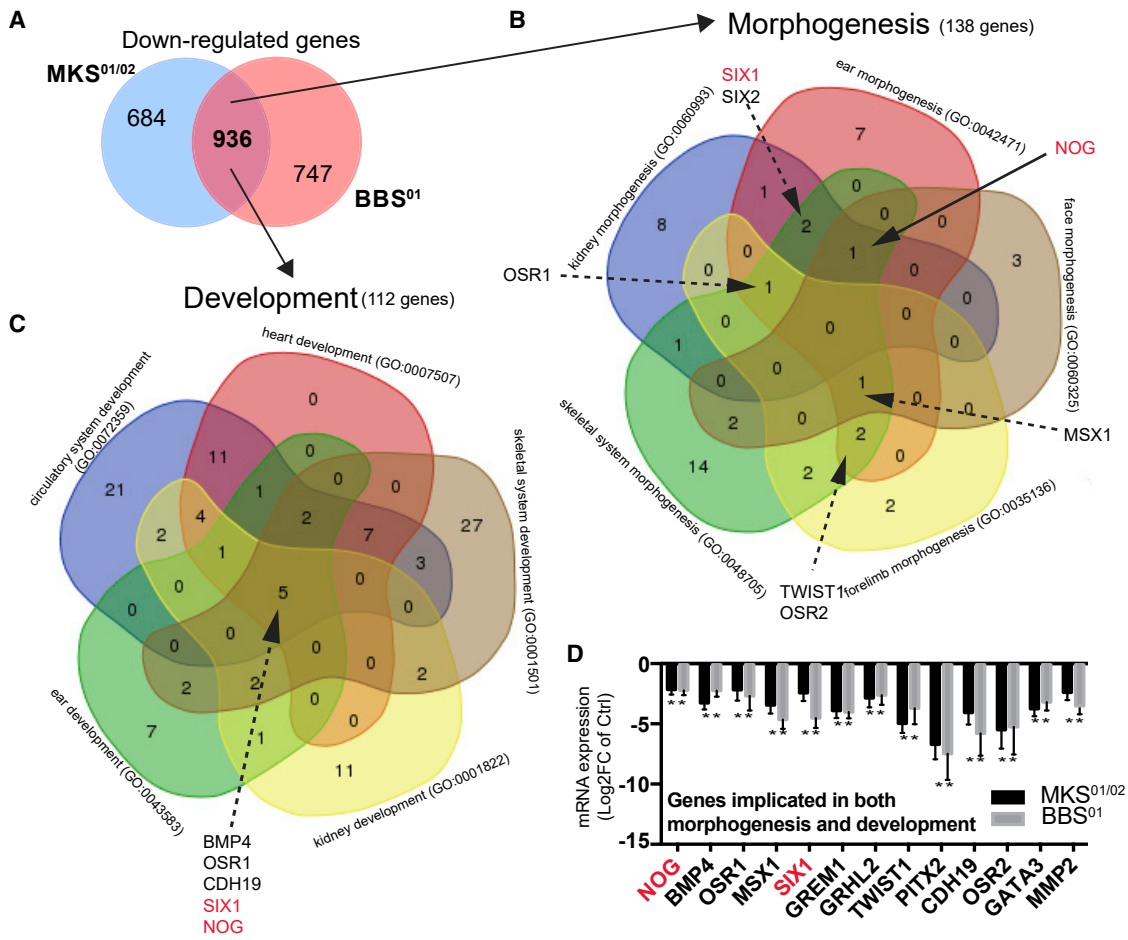

Figure 3. Reduced Expression of Genes Involved in Development and Morphogenesis

(A) Venn diagrams showing the intersection of significant genes differentially downregulated between $MKS^{01/02}$ (blue) and BBS^{01} RSs (red).

(B and C) Venn diagrams showing the intersection of significative downregulated genes belonging to GO groups involved in the morphogenesis (B) or in the development (C) of five organs/systems commonly affected in both MKS and BBS (log2FC > 2; $p < 0.05$).

(D) Gene expression levels in BBS^{01} and $MKS^{01/02}$ RSs at DIV60 of genes implicated in both development and morphogenesis. In red, the genes common to all five developmental groups with a role also in morphogenesis.

All values are means ± SEM. *$p < 0.05$, Student's unpaired t test.

S1H). Hence, we could observe by immunoblot the presence of MKS3 in $Ctrl^{01}$, $MKS^{01/02}$, and $BBS^{01/02}$ RSs, and MKS3 levels were even slightly increased in MKS^{01} RSs (Figure 5H). Using antibodies against Centriolin and MKS3, we performed confocal immunofluorescence imaging and 3D reconstruction on dissociated control PRs. We observed three different configurations between Centriolin and MKS3: BBs and daughter centrioles surrounding MKS3 (F′); MKS3 linked to the centriole (F″); and unlinked MKS3 and Centriolin (F‴) (Figure 5F). Notably, while we observed that MKS3 was often in close association with Centriolin in control and BBS^{01} PRs (Pearson's coefficient correlation = 0.29 and 0.23), this association was near absent in MKS^{01} PRs (Pearson's coefficient correlation = 0.06) (Figures 5E–5G). These results suggested defective interaction of MKS3 with the centriole in MKS^{01} PRs, possibly leading to the production of supernumerary centrioles (see model in Figure S6).

MKS^{01} PRs Have Smaller but Supernumerary Cilia and Present Abnormal Accumulations of Ciliary Proteins

Using an antibody against acetylated α-tubulin, we found that supernumerary centrioles in MKS^{01} PRs were also associated with an increasing number of cilia (Figures 6A–6C). This phenotype was not observed in BBS^{01} PRs. We performed quantitative analyses of the images using IMARIS, which revealed that, although more numerous, cilia in MKS^{01} PRs were shorter and thinner than normal (Figures

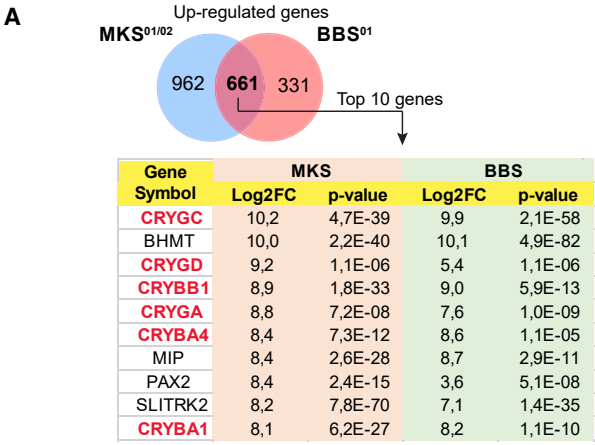

Gene Symbol	MKS		BBS	
	Log2FC	p-value	Log2FC	p-value
CRYGC	10,2	4,7E-39	9,9	2,1E-58
BHMT	10,0	2,2E-40	10,1	4,9E-82
CRYGD	9,2	1,1E-06	5,4	1,1E-06
CRYBB1	8,9	1,8E-33	9,0	5,9E-13
CRYGA	8,8	7,2E-08	7,6	1,0E-09
CRYBA4	8,4	7,3E-12	8,6	1,1E-05
MIP	8,4	2,6E-28	8,7	2,9E-11
PAX2	8,4	2,4E-15	3,6	5,1E-08
SLITRK2	8,2	7,8E-70	7,1	1,4E-35
CRYBA1	8,1	6,2E-27	8,2	1,1E-10

(legend on next page)

6D and 6E). Some rare giant cilia resembling a fusion of different cilia were also observed. The number of observed cilia was normal in undifferentiated iPSCs from MKS^{01} patients, suggesting cell-type specificity for this phenotype (Figures S5F–S5H). RPGR mostly labels the BBs of the CC (Figure 6F) (He et al., 2008). Using confocal microscopy and 3D reconstruction, we observed that control RSs presented a relatively uniform immuno-labeling for RPGR proximal to the PNA-positive OS (Figure 6G). In contrast, MKS^{01} RSs were disorganized, as revealed by the unequal distribution of PNA. Furthermore, the signal for RPGR was mislocalized and tended to accumulate in aggregates. RPGR was also mislocalized in RSs from the BBS^{01} patient (Figure 6G). These results suggested supernumerary cilia, abnormal retinal tissue morphogenesis, and aggregation of ciliary proteins in MKS PRs.

BBS PRs Display Mitotic Spindle Checkpoint Activation and Genomic Instability

Significantly upregulated genes in BBS^{01} RSs included markers of mitotic spindle checkpoint and regulation of microtubule cytoskeleton organization (Figures 7A, 7B, and S7B), suggesting possible genomic instability during mitosis. On the other hand, we observed downregulation of genes involved in extracellular matrix organization and tube development (Figure S7D). DIV15 PR progenitors were analyzed using specific antibodies. We found that the number of cells expressing the DNA damage-response markers, γH2Ax and 53BP1, and the activated mitotic checkpoint protein, pCHK2, were increased in BBS$^{01/02}$ samples, but not in control or MKS$^{01/02}$ samples (Figures 7C–7G and S7E–S7H). This phenotype was, however, generally more severe in the BBS^{01} case than in the BBS^{02} case. We also observed the presence of very large nuclei in BBS$^{01/02}$ PRs that were also γH2Ax and pCHK2-positive, suggesting possible arrest in the G2/M phase of the cell cycle. γH2Ax, a marker of DNA double-strand breaks, was also detected by immunoblot on whole-cell extracts in BBS^{01} RSs at DIV60 of differentiation, but not in control or MKS^{01} RSs (Figure 7H). Consistently, micronuclei, nuclear bridges, mitotic catastrophe, and nuclei having multipolar or monopolar spindles, were more frequent in BBS^{01} PRs progenitors than in the MKS^{01} or control one. Nuclear bridges were detected in all conditions but tended to be more abundant in BBS^{01} PRs. Mitotic catastrophes were also significantly higher in BBS^{01} than in control cells, but they were also present in MKS^{01} cells (Figure 7I). We concluded that, although MKS and BBS PRs shared a broad number of molecular and cellular alterations, they also displayed unique anomalies that may help explain the distinct phenotypes characterizing these disorders.

DISCUSSION

We generated iPSCs from control and ciliopathy cases and differentiated them into polarized 3D-adherent RSs that could recapitulate normal PR development and disease state, respectively. By WGS, we identified mutations in *BBS10* (BBS^{01} and BBS^{02} patients) and *TMEM67* (MKS^{01} case). Using RNA-seq analyses and high-resolution fluorescence microscopy, we were able to identify and study retinal developmental anomalies and PR degeneration processes that characterized MKS and BBS. Importantly, we could also distinguish specific pathological features that were either common or unique to the two syndromes.

Previous reports based on rare genetic cases suggested that BBS and MKS may represent a "unique disease" with

Figure 4. Induction and Accumulation of Crystallins in MKS and BBS RSs

(A) Venn diagrams showing the intersection of significant genes differentially upregulated between MKS$^{01/02}$ (blue) and BBS^{01} RSs (red) (log2FC > 2; p < 0.05), and the top 10 upregulated genes common to the two groups with their respective log2FC and p value for each group. Genes that are members of the crystallin family are highlighted in red.

(B) Immunoblot on extracts from undifferentiated iPSCs and RSs.

(C) Immunofluorescence (IF) representative images showing CRYBB1 and CRYBB3 accumulation in MKS$^{01/02}$ and BBS^{01} CRX-positive cells at DIV45. Note the extracellular and intracellular accumulation of crystallin (white arrows). Scale bars, 10 μm.

(D) TEM representative images of RSs at DIV60. BBs (black arrowheads) and dead cells (white arrowheads). For each condition at the bottom some high-magnification images. In Ctrl^{04} we can observe IS structure with high density of mitochondria, BBs near the apical surface, and marked gap junction. A beginning of OS with stack-like structures (black arrows) can be observed beyond the apical surface. Vesicles with laminar material are also observed near the surface. Big vesicles similar to lysosomes were particularly abundant in MKS RSs. M, mitochondria; A, apoptotic cells; N, necrotic cells.

(E–G) Quantification of the percentage of total dead cells (E), apoptotic (F), and necrotic (G) cells observed by TEM at DIV60 (n = 3–4 fields for condition, an average of 24 cells for field.

(H) IF representative images in dissociated cells culture at DIV20. Scale bar, 50 μm.

(I) Quantification of the percentage of TUNEL-positive cells over total nuclei at DIV20 (n = 4–5 fields for condition, an average of 85 cells for field).

n = 3 independent biological replicates for all experiments. All values are means ± SEM. *p < 0.05, **p < 0.01, ***p < 0.001 by one-way ANOVA test.

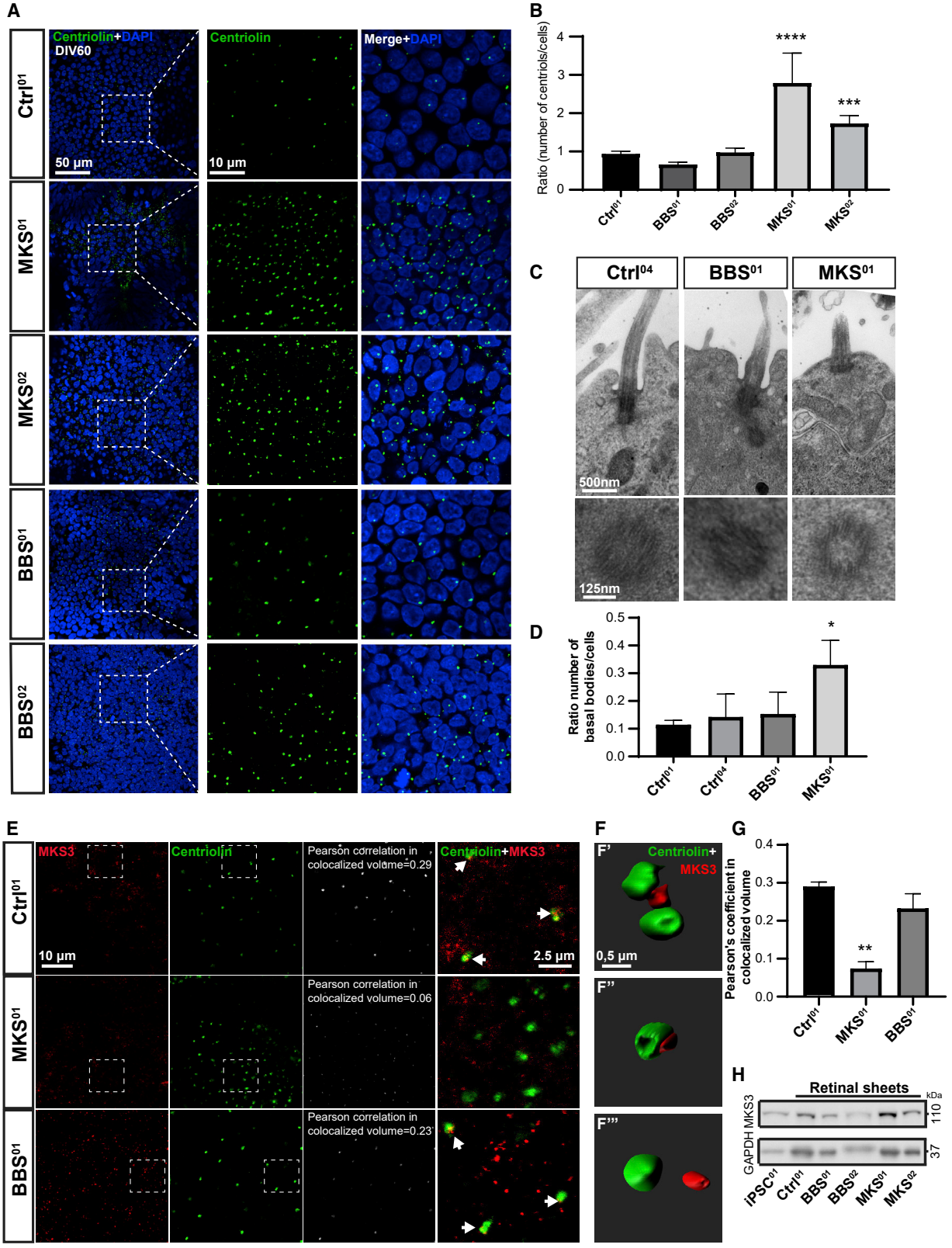

(legend on next page)

two different degrees of severity (Brunham, 2009; Leitch et al., 2008). Using our *in vitro* model, we found that 60% of deregulated genes in BBS^{01} PRs and 49% of those in MKS$^{01/02}$ PRs were common between both diseases, although BBS and MKS cases studied here carried mutations in unrelated genes. Brain, eye, and bone malformations as well as polydactyly are common to MKS and BBS. Hence, we found deregulation of hundreds of neurodevelopmental genes, most of them common to both ciliopathies. WNT, NOTCH, and HOX signaling pathways were highly affected, consistent with the essential function of WNT and NOTCH in neural development, and with the role of the *HOX* gene cluster in axial skeleton development and digit formation (Sheth et al., 2012; Tan et al., 2013; Wheway et al., 2013). Unexpectedly, we observed significant downregulation of *NOG*, *BMP*, *SIX1*, *MSX1*, *TWIST*, *OSR1*, and *PITX2*. *NOG* and *BMP* are important for nervous system, muscle, and bone development, while the others are required for the differentiation of intermediate mesoderm-derivative (gonads and kidneys) and limb buds (*OSR1*), in epithelial-mesenchymal transition (*TWIST*), in the development of the neck, ears, and kidneys (*SIX1*), and of oral structures (*MSX1*). *PITX2* is involved in the establishment of the left-right axis and morphogenesis of many organs (Campione et al., 1999; Zacharias et al., 2011). Mutations in *PITX2* are associated with Axenfeld-Rieger syndrome, iridogoniodysgenesis syndrome, and sporadic cases of Peters anomaly, revealing its important role in eye development (Kozlowski and Walter, 2000). Notably, polydactyly, craniofacial, neural, retinal, ocular, skeletal, and kidney anomalies are commonly observed in syndromic ciliopathies (Brunham, 2009; Novarino et al., 2011). Thus, developmental defects observed in peripheral organs and musculoskeletal structures of MKS and BBS patients were revealed in our gene expression profile analyses of RSs.

We found upregulation of several apoptotic genes and genes of the beta- and gamma-crystallin families in both MKS and BBS RSs. Alpha-crystallins are known to operate as molecular chaperones for misfolded proteins and can be found in ubiquitin-associated inclusions in neurodegenerative diseases (Lowe et al., 2001; Thornell and Aquilina, 2015). In contrast, the function of beta- and gamma-crystallins in non-lens tissue is not well understood. Some studies have linked the expression of beta- and gamma-crystallins to retinal diseases. It has also been observed that gamma- and beta-crystallin production increases before PR cell death in animal models of retinitis pigmentosa and light-induced retinal degeneration (Fort et al., 2009; Organisciak et al., 2006; Piri et al., 2007; Sakaguchi et al., 2003). βB2-Crystallin (*CRYBB2*) was shown to be strongly expressed in regenerating ganglion cells where it may promote axonal regrowth (Liedtke et al., 2007). Thus, although the exact role of crystallins in neurodegenerative contexts remains to be clarified, our findings reveal robust activation of this pathway in PRs from ciliopathy patients.

In MKS^{01} PRs, we observed near absent co-localization of MKS3 with Centriolin, which may explain the presence of supernumerary centrioles. Cilia were also shorter and thinner than normal, suggesting cilia degeneration and/or abnormal formation and maintenance. Notably, it was shown that, in mouse renal-tubule epithelial cells, reducing the level of MKS3 using small interfering RNA impaired the number of cilia, whereas its complete loss caused elongated cilia (Cook et al., 2009). Multi-ciliated cells were also observed in MKS patients and in a rat model of MKS3 (Gattone et al., 2004). We also found that MKS^{01} RSs were highly disorganized and that the signal for RPGR was mislocalized and tended to accumulate in aggregates. BBS^{01} cells also showed abnormal RPGR localization. Unlike MKS^{01} PRs, however, RPGR was generally mislocalized at the basement of BBS^{01} PRs, suggesting abnormal transport or docking to the BB. This reveals both similarities and differences between the two syndromes. Moreover, genes implicated in canonical WNT signaling were upregulated, and this was apparently at the expense of the non-canonical one. In polarized cells, the cilium grows

Figure 5. Supernumerary Centrioles in MKS PRs

(A) IF images of PRs at DIV60. Composed image from two focal planes (DAPI and Centriolin). Scale bars, 50 μm (left), 10 μm (right).

(B) Quantification of the number of centrioles (Centriolin) per cells at DIV60 (n = 4 fields for condition, an average of 113 cells for a field).

(C) TEM representative images of cilia and BBs and its section (bottom).

(D) Quantification of the ratio of BBs/cell per field by TEM. N = 3–4 images for condition an average of 24 cells for a field.

(E) IF images of dissociated PRs at DIV60. The white channel represents colocalized volume between Centriolin and MKS3 with the respective Pearson correlation value quantified in (G). On the right, high-magnification images of the respective dashed square in each condition.

(F) Representative surface rendering from 3D z stack reconstruction of the three conformations observed between Centriolin and MKS3: BBs and daughter centrioles surrounding MKS3 (F′), MKS3 linked to Centriolin (F″), and MKS3 and Centriolin unbound (F‴). Scale bar, 0.5 μm.

(G) Pearson correlation of colocalized volume between Centriolin and MKS3 related to (E).

(H) Immunoblot on extracts from iPSCs and RSs.

n = 3 independent biological replicates for all experiments. All values are means ± SEM. *p < 0.05, **p < 0.01, ***p < 0.001, ****p < 0.0001 by one-way ANOVA test.

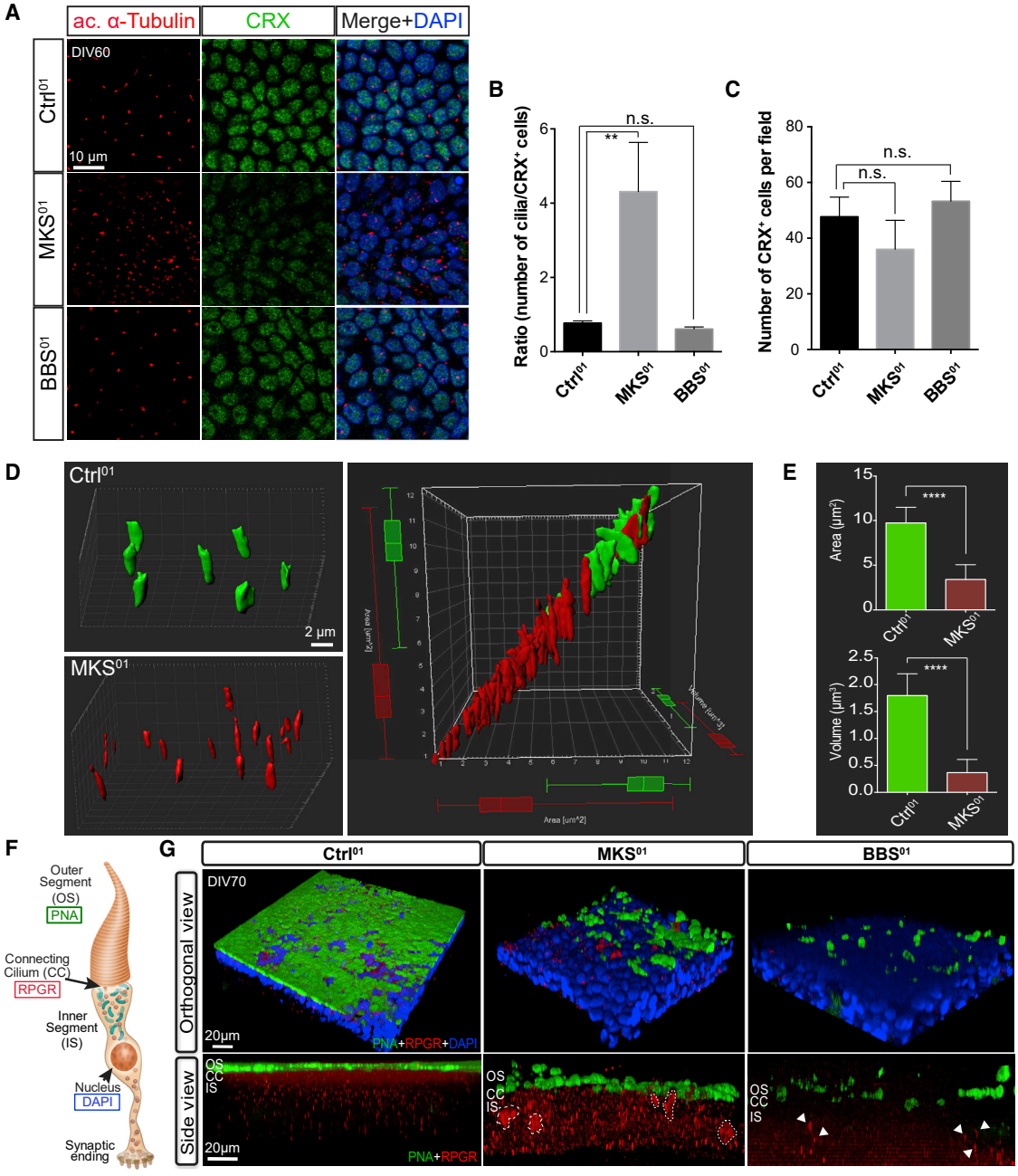

Figure 6. Supernumerary Cilia and Aggregation of Ciliary Proteins in MKS^{01} PRs

(A) IF of PRs at DIV60. Composed image from two focal planes (DAPI and acetyl-α-tubulin). Scale bar, 10 μm.

(B and C) Quantification of the number of cilia (acetyl-α-tubulin) per cells (B) and the number of CRX-positive cells per field (C) in cells at DIV60 (n = 4 fields for condition, an average of 53 cells for a field).

(D) Surface rendering 3D reconstruction from confocal z stack images of Ctrl^{01} (green) and MKS^{01} (red) based on acetyl-α-tubulin staining (left). Scale bar, 2 μm. A 3D plot of cilia (cilia from three images put together for each condition) based on area and volume (right). Notice how control cilia clustered together while MKS^{01} cilia are more heterogeneous, smaller, and more abundant (n = 2 independent experiments).

(E) Quantification of area and volume of Ctrl^{01} and MKS^{01} cilia (ctrl n = 20; MKS n = 47).

(F) Representation of cone PRs with reference to OS, CC, IS, and nucleus, and the localization of the markers used in (G).

(legend continued on next page)

at the apical side. During ciliogenesis, planar cell polarity and apical-basal polarity are necessary for docking of the centrioles at the plasma membrane, and for correct formation and maintenance of PR BBs (Kim et al., 2010; Oishi et al., 2006). Taken as a whole, these observations suggest that hallmarks of the MKS phenotype previously reported in MKS patients and animal models were recapitulated at the cellular and molecular levels in $MKS^{01/02}$ RSs. Furthermore, we described for the first time the presence of supernumerary cilia and centrioles in $MKS^{01/02}$ PRs, which was associated with reduced co-localization of MKS3 with Centriolin in the MKS^{01} case, suggesting deficient interaction of the mutant MKS3 protein with centrioles. In the MKS^{02} case, which does not carry mutations in *TMEM67*, the number of centrioles/cell was about 2-fold higher than in controls and $BBS^{01/02}$ cases but was less severe than in MKS^{01}. It is not surprising thus that despite carrying mutations in different genes, MKS cases show highly related phenotypes at the cellular and molecular levels.

Previous reports have described cilia proteins with cilia-independent functions, including mitotic spindle generation and mitotic process regulation (Hua and Ferland, 2018; Vertii et al., 2015; Yuan and Sun, 2013). Unexpectedly, we found genomic instability in $BBS^{01/02}$ retinal progenitors and PRs, with the most prominent feature being the activation of the mitotic spindle checkpoint. This suggests a new and essential role of BBS10 in microtubule cytoskeleton organization during mitosis.

In summary, we have produced iPSCs from control, and MKS and BBS cases, and differentiated them into RSs, allowing recapitulation of normal and pathological human retinal and PRs development *in vitro*. Molecular and cell biological analyses further revealed known and novel disease mechanisms associated with retinal ciliopathies, opening potentially new avenues for disease treatment.

EXPERIMENTAL PROCEDURES

iPSC Generation and Characterization

Human PSCs were used in accordance with the Canadian Institute Health Research (CIHR) guidelines and approved by the "Comité de Surveillance de la Recherche sur les Cellules Souches" of the CIHR and the Maisonneuve-Rosemont Hospital Ethic Committee. MKS and BBS fibroblasts were obtained from clinically diagnosed individuals (Coriell Biorepository). These were reprogrammed with the Yamanaka factors, *OCT4*, *SOX2*, *KLF4*, and *c-MYC*, using the pMIG vector set. Stem cells were grown on MEF feeder layers (Global Stem Cell GSC-6001G) in iPSC medium. To generate teratomas, $\sim 3 \times 10^6$ undifferentiated iPSCs were implanted beneath the neck scruff of non-obese diabetic-severe combined immunodeficiency immunodeficient mice. Tumors were harvested 12 weeks later and processed for histology analysis. See Supplemental Information for details.

Differentiation of Human ESCs and iPSCs into RSs

iPSCs and ESCs were dissociated using ReLeSR (STRMCELL Technologies, cat. no. 05,872) and platted on growth factor reduced Matrigel (Corning, no. 356231) in StemFlex cell medium (Gibco, no. A3349401) supplemented with ROCK-inh (Y-27632; 10 μM, Cayman Chemical, no. 10005583). When PSCs reach full confluence, the medium was switched to differentiation medium supplemented with 60 ng/mL of recombinant COCO as described in Zhou et al. (2015). See Supplemental Information for details.

RNA-Seq and WGS Analyses

RNA-seq libraries were prepared using Ion Total RNA-Seq Kit v.2. Libraries were sequenced onto P1 chips from Ion Torrent as unpaired to reach 40 million reads for each sample. Raw sequencing files (FASTQ) were validated using FASTQC v.0.11.7.

Base calling for WGS was performed using Illumina HiSeq Analysis Software (v.2—2.5.55.1311). Reads were mapped to the b37 reference sequence. See Supplemental Information for details.

Statistical Analysis

Statistical analysis was performed using GraphPad software (Prism 6). Statistical differences were analyzed using the Student's t test for unpaired samples. Values are representative of at least three experiments. When comparisons were made using independent samples of equal size and variance following a normal distribution, significance was assessed using an unpaired two-sided Student's t test. Where several groups were compared, significance was assessed by ANOVA and adjusted for multiple comparisons using the Bonferroni correction. Differential expression was assayed using a log2 fold change statistical algorithm or one-way ANOVA with a p value cutoff at 0.05. For gene ontology, a false discovery rate cutoff of 0.01 was applied.

ACCESSION NUMBERS

RNAseq Data was deposited in the GEO: GSE133247. WGS data were deposited in BioSample database: SAMN13656497; SAMN13656498

SUPPLEMENTAL INFORMATION

Supplemental Information can be found online at https://doi.org/10.1016/j.stemcr.2020.02.005.

(G) 3D z stack reconstruction of RSs from IF images at DIV70. Dotted lines, intracellular aggregates of RPGR. White arrows, RPGR not polarized to the apical zone. Scale bars, 20 μm.

n = 3 independent biological replicates for all experiments. All values are means ± SEM. **p < 0.01, ****p < 0.0001, Student's unpaired t test.

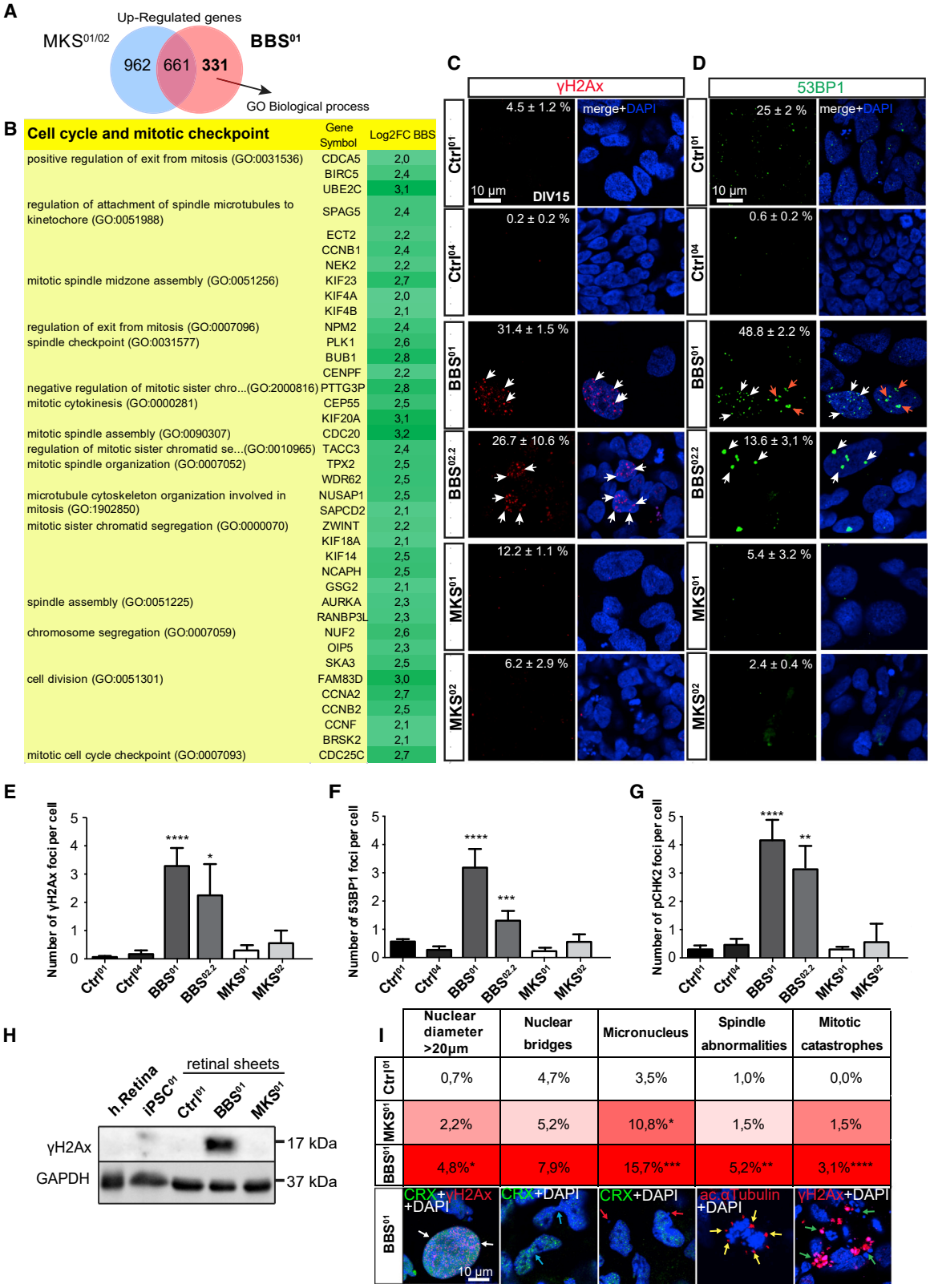

(legend on next page)

AUTHOR CONTRIBUTIONS

A.B. and G.B. wrote the article. A.B. did the cell culture and most of the experiments and analyses. B.S.F. generated and characterized MKS and BBS iPSc lines and helped write the manuscript. E.H. helped identify the mutations through WGS and helped write the manuscript. A.F. contributed to the bioinformatic analysis of the RNA-seq and helped write the manuscript. R.H. contributed to the bioinformatic analysis of the RNA-seq and to the quantifications of DNA damage and helped write the manuscript.

ACKNOWLEDGMENTS

This work was supported by grants from the Foundation Fighting Blindness Canada, Natural Sciences and Engineering Research Council of Canada (2017-05504), and Maisonneuve-Rosemont Hospital Foundation in Montreal, Canada. A.F., R.H., and A.B. were supported by fellowships from the Molecular Biology Program of Université de Montréal. Work in the Freedman laboratory was supported by NIH Award K01DK102826, United States. We thank Steve Breault, Anna Baccei, and Joseph Bonventre for assistance with scanning electron microscopy and stem cell culture, Eric Pierce, Marc Consugar, and Erika Tavares for the mutational analysis and WGS, and Fabien Martinel for the photoreceptor graphics. G.B. and A.F. are co-founders of StemAxon and members of its scientific advisory board. The corporation was not involved in this study.

Received: July 8, 2019
Revised: February 10, 2020
Accepted: February 11, 2020
Published: March 10, 2020

REFERENCES

Aboshiha, J., Dubis, A.M., Carroll, J., Hardcastle, A.J., and Michaelides, M. (2016). The cone dysfunction syndromes. Br. J. Ophthalmol. *100*, 115–121.

Adams, M., Simms, R.J., Abdelhamed, Z., Dawe, H.R., Szymanska, K., Logan, C.V., Wheway, G., Pitt, E., Gull, K., Knowles, M.A., et al. (2012). A meckelin-filamin A interaction mediates ciliogenesis. Hum. Mol. Genet. *21*, 1272–1286.

Adams, N.A., Awadein, A., and Toma, H.S. (2007). The retinal ciliopathies. Ophthal. Genet. *28*, 113–125.

Ahmed, M., Xu, J., and Xu, P.-X. (2012). EYA1 and SIX1 drive the neuronal developmental program in cooperation with the SWI/SNF chromatin-remodeling complex and SOX2 in the mammalian inner ear. Development *139*, 1965–1977.

Álvarez-Satta, M., Castro-Sánchez, S., and Valverde, D. (2017). Bardet-Biedl syndrome as a chaperonopathy: dissecting the major role of chaperonin-like BBS proteins (BBS6-BBS10-BBS12). Front. Mol. Biosci. *4*, 1–7.

Breuer, D.K., Yashar, B.M., Filippova, E., Hiriyanna, S., Lyons, R.H., Mears, A.J., Asaye, B., Acar, C., Vervoort, R., Wright, A.F., et al. (2002). A comprehensive mutation analysis of RP2 and RPGR in a North American cohort of families with X-linked retinitis pigmentosa. Am. J. Hum. Genet. *70*, 1545–1554.

Brunham, L. (2009). Cilia get serious: Meckel-Gruber and Bardet-Biedl syndromes represent a spectrum of allelic disorders. Clin. Genet. *75*, 40–41.

Burnicka-Turek, O., Steimle, J.D., Huang, W., Felker, L., Kamp, A., Kweon, J., Peterson, M., Reeves, R.H., Maslen, C.L., Gruber, P.J., et al. (2016). Cilia gene mutations cause atrioventricular septal defects by multiple mechanisms. Hum. Mol. Genet. *25*, 3011–3028.

Campione, M., Steinbeisser, H., Schweickert, A., Deissler, K., van Bebber, F., Lowe, L.A., Nowotschin, S., Viebahn, C., Haffter, P., Kuehn, M.R., et al. (1999). The homeobox gene Pitx2: mediator of asymmetric left-right signaling in vertebrate heart and gut looping. Development *126*, 1225–1234.

Chang, P., Giddings, T.H., Winey, M., and Stearns, T. (2003). ϵ-Tubulin is required for centriole duplication and microtubule organization. Nat. Cell Biol. *5*, 71–76.

Cook, S.A., Collin, G.B., Bronson, R.T., Naggert, J.K., Liu, D.P., Akeson, E.C., and Davisson, M.T. (2009). A mouse model for Meckel syndrome type 3. J. Am. Soc. Nephrol. *20*, 753–764.

Delous, M., Baala, L., Salomon, R., Laclef, C., Vierkotten, J., Tory, K., Golzio, C., Lacoste, T., Besse, L., Ozilou, C., et al. (2007). The ciliary gene RPGRIP1L is mutated in cerebello-oculo-renal syndrome (Joubert syndrome type B) and Meckel syndrome. Nat. Genet. *39*, 875–881.

Figure 7. Activation of the Mitotic Spindle Checkpoint and Accumulation of DNA Damage in BBS PRs

(A) Venn diagrams showing the intersection of significant genes differentially upregulated in $MKS^{01/02}$ (blue) and BBS^{01} RSs (red) (log2FC > 2; p < 0.05).

(B) Gene ontology enrichment analyses of BBS^{01}-specific differentially upregulated genes. The main GO group and subgroups are shown. Some representative genes and the respective log2FC (p < 0.05) are indicated for each category.

(C and D) IF images of PR progenitors at DIV15 for γH2Ax (C), and 53BP1 (D). The percentage of positive cells (more than three foci per cell) are indicated on the respective images (average n = 253 cells for each condition). Scale bars, 10 μm.

(E–G) Quantification of the average number of foci per cell for γH2Ax (E), 53BP1 (F), and pCHK2 (G) in PR progenitors at DIV15 (n > 3 fields for condition, an average of 84 cells for a field).

(H) Immunoblot on extracts from undifferentiated iPSCs and RSs at DIV60.

(I) Representative images for common mitotic abnormalities and the respective percentages of cells for each condition in PR progenitors at DIV15. White arrows, giant nucleus; blue arrows, nuclear bridge; red arrows, micronuclei; yellow arrows, multifocal spindle; green arrows, fragmented nuclei strongly marked by the anti-γH2Ax antibody. Scale bars, 10 μm.

n = 3 independent biological replicates for all experiments. All values are means ± SEM. *p < 0.05, **p < 0.01, ***p < 0.001, ****p < 0.0001, Student's unpaired t test.

Fort, P.E., Freeman, W.M., Losiewicz, M.K., Singh, R.S.J., and Gardner, T.W. (2009). The retinal proteome in experimental diabetic retinopathy: up-regulation of crystallins and reversal by systemic and periocular insulin. Mol. Cell. Proteomics *8*, 767–779.

Gattone, V.H., Tourkow, B.A., Trambaugh, C.M., Yu, A.C., Whelan, S., Phillips, C.L., Harris, P.C., and Peterson, R.G. (2004). Development of multiorgan pathology in the wpk rat model of polycystic kidney disease. Anat. Rec. *277A*, 384–395.

Goodnough, L.H., Dinuoscio, G.J., and Atit, R.P. (2016). Twist1 contributes to cranial bone initiation and dermal condensation by maintaining Wnt signaling responsiveness. Dev. Dyn. *245*, 144–156.

Grandy, R., Tomaz, R.A., and Vallier, L. (2019). Modeling disease with human inducible pluripotent stem cells. Annu. Rev. Pathol. Mech. Dis. *14*, 449–468.

Gupta, G.D., Coyaud, É., Gonçalves, J., Mojarad, B.A., Liu, Y., Wu, Q., Gheiratmand, L., Comartin, D., Tkach, J.M., Cheung, S.W.T., et al. (2015). A dynamic protein interaction landscape of the human centrosome-cilium interface. Cell *163*, 1484–1499.

He, S., Parapuram, S.K., Hurd, T.W., Behnam, B., Margolis, B., Swaroop, A., and Khanna, H. (2008). Retinitis pigmentosa GTPase regulator (RPGR) protein isoforms in mammalian retina: insights into X-linked Retinitis Pigmentosa and associated ciliopathies. Vis. Res. *48*, 366–376.

Hoshino, A., Ratnapriya, R., Brooks, M.J., Chaitankar, V., Wilken, M.S., Zhang, C., Starostik, M.R., Gieser, L., La Torre, A., Nishio, M., et al. (2017). Molecular anatomy of the developing human retina. Dev. Cell *43*, 763–779.e4.

Hua, K., and Ferland, R.J. (2018). Primary cilia proteins: ciliary and extraciliary sites and functions. Cell. Mol. Life Sci. *75*, 1521–1540.

HUGO (2019). Cilia and flagella associated (CFAP) gene family. HUGO Gene Nomenclature Committee. URL: https://www.genenames.org/data/genegroup/#!/group/1491

Kamachi, Y., Uchikawa, M., Tanouchi, A., Sekido, R., and Kondoh, H. (2001). Pax6 and SOX2 form a co-DNA-binding partner complex that regulates initiation of lens development. Genes Dev. *15*, 1272–1286.

Khanna, H. (2015). Photoreceptor sensory cilium: traversing the ciliary gate. Cells *4*, 674–686.

Kim, S.K., Shindo, A., Park, T.J., Oh, E.C., Ghosh, S., Gray, R.S., Lewis, R.A., Johnson, C.A., Attie-Bittach, T., Katsanis, N., et al. (2010). Planar cell polarity acts through septins to control collective cell movement and ciliogenesis. Science *329*, 1337–1340.

Kozlowski, K., and Walter, M.A. (2000). Variation in residual PITX2 activity underlies the phenotypic spectrum of anterior segment developmental disorders. Hum. Mol. Genet. *9*, 2131–2139.

Kyttälä, M., Tallila, J., Salonen, R., Kopra, O., Kohlschmidt, N., Paavola-Sakki, P., Peltonen, L., and Kestilä, M. (2006). MKS1, encoding a component of the flagellar apparatus basal body proteome, is mutated in Meckel syndrome. Nat. Genet. *38*, 155–157.

Leitch, C.C., Zaghloul, N.A., Davis, E.E., Stoetzel, C., Diaz-Font, A., Rix, S., Alfadhel, M., Lewis, R.A., Eyaid, W., Banin, E., et al. (2008). Hypomorphic mutations in syndromic encephalocele genes are associated with Bardet-Biedl syndrome. Nat. Genet. *40*, 443–448.

Li, M., Jia, C., Kazmierkiewicz, K.L., Bowman, A.S., Tian, L., Liu, Y., Gupta, N.A., Gudiseva, H.V., Yee, S.S., Kim, M., et al. (2014). Comprehensive analysis of gene expression in human retina and supporting tissues. Hum. Mol. Genet. *23*, 4001–4014.

Li, X., Ohgi, K.A., Zhang, J., Krones, A., Bush, K.T., Glass, C.K., Nigam, S.K., Aggarwal, A.K., Maas, R., Rose, D.W., et al. (2003). Eya protein phosphatase activity regulates Six1-Dach-Eya transcriptional effects in mammalian organogenesis. Nature *426*, 247–254.

Liedtke, T., Schwamborn, J.C., Schröer, U., and Thanos, S. (2007). Elongation of axons during regeneration involves retinal crystallin beta b2 (crybb2). Mol. Cell. Proteomics *6*, 895–907.

Loncarek, J., and Bettencourt-Dias, M. (2018). Building the right centriole for each cell type. J. Cell Biol. *217*, 823–835.

Lowe, J., Mayer, J., Landon, M., and Layfield, R. (2001). Ubiquitin and the molecular pathology of neurodegenerative diseases. Adv. Exp. Med. Biol. *487*, 169–186.

Ma, L., Wang, Y., Hui, Y., Du, Y., Chen, Z., Feng, H., Zhang, S., Li, N., Song, J., Fang, Y., et al. (2019). WNT/NOTCH pathway is essential for the maintenance and expansion of human MGE progenitors. Stem Cell Reports *12*, 934–949.

Marszalek, J.R., Liu, X., Roberts, E.A., Chui, D., Marth, J.D., Williams, D.S., and Goldstein, L.S.B. (2000). Genetic evidence for selective transport of opsin and arrestin by kinesin-II in mammalian photoreceptors. Cell *102*, 175–187.

May-Simera, H.L., and Kelley, M.W. (2012). Cilia, Wnt signaling, and the cytoskeleton. Cilia *1*, 7.

Navarro Quiroz, E., Navarro Quiroz, R., Ahmad, M., Gomez Escorcia, L., Villarreal, J.L., Fernandez Ponce, C., and Aroca Martinez, G. (2018). Cell signaling in neuronal stem cells. Cells *7*. https://doi.org/10.3390/cells7070075.

Nishimura, D.Y., Fath, M., Mullins, R.F., Searby, C., Andrews, M., Davis, R., Andorf, J.L., Mykytyn, K., Swiderski, R.E., Yang, B., et al. (2004). Bbs2-null mice have neurosensory deficits, a defect in social dominance, and retinopathy associated with mislocalization of rhodopsin. Proc. Natl. Acad. Sci. U S A *101*, 16588–16593.

Nonaka, S., Tanaka, Y., Okada, Y., Takeda, S., Harada, A., Kanai, Y., Kido, M., and Hirokawa, N. (1998). Randomization of left-right asymmetry due to loss of nodal cilia generating leftward flow of extraembryonic fluid in mice lacking KIF3B motor protein. Cell *95*, 829–837.

Novarino, G., Akizu, N., and Gleeson, J.G. (2011). Modeling human disease in humans: the ciliopathies. Cell *147*, 70–79.

Oishi, I., Kawakami, Y., Raya, Á., Callol-Massot, C., and Belmonte, J.C.I. (2006). Regulation of primary cilia formation and left-right patterning in zebrafish by a noncanonical Wnt signaling mediator, duboraya. Nat. Genet. *38*, 1316–1322.

OMIM (2019a). OMIM Entry Search—MECKEL-GRUBER SYNDROME 1 # 249000. URL: https://omim.org/entry/249000

OMIM (2019b). OMIM Entry Search—BARDET-BIEDL SYNDROME 1 # 209900. URL: https://omim.org/entry/209900

Organisciak, D., Darrow, R., Gu, X., Barsalou, L., and Crabb, J.W. (2006). Genetic, age and light mediated effects on crystallin protein expression in the retina. Photochem. Photobiol. *82*, 1088.

Ou, Y.Y., Mack, G.J., Zhang, M., and Rattner, J.B. (2002). CEP110 and ninein are located in a specific domain of the centrosome associated with centrosome maturation. J. Cell Sci. *115*, 1825–1835.

Paradowska-Stolarz, A. (2015). MSX1 gene in the etiology orofacial deformities. Postepy Hig. Med. Dosw. (Online) *69*, 1499–1504.

Pazour, G.J., Baker, S.A., Deane, J.A., Cole, D.G., Dickert, B.L., Rosenbaum, J.L., Witman, G.B., and Besharse, J.C. (2002). The intraflagellar transport protein, IFT88, is essential for vertebrate photoreceptor assembly and maintenance. J. Cell Biol. *157*, 103–114.

Piri, N., Song, M., Kwong, J.M.K., and Caprioli, J. (2007). Modulation of alpha and beta crystallin expression in rat retinas with ocular hypertension-induced ganglion cell degeneration. Brain Res. *1141*, 1–9.

Reiter, J.F., Blacque, O.E., and Leroux, M.R. (2012). The base of the cilium: roles for transition fibres and the transition zone in ciliary formation, maintenance and compartmentalization. EMBO Rep. *13*, 608–618.

Sahly, I., Dufour, E., Schietroma, C., Michel, V., Bahloul, A., Perfettini, I., Pepermans, E., Estivalet, A., Carette, D., Aghaie, A., et al. (2012). Localization of Usher 1 proteins to the photoreceptor calyceal processes, which are absent from mice. J. Cell Biol. *199*, 381–399.

Sakaguchi, H., Miyagi, M., Darrow, R.M., Crabb, J.S., Hollyfield, J.G., Organisciak, D.T., and Crabb, J.W. (2003). Intense light exposure changes the crystallin content in retina. Exp. Eye Res. *76*, 131–133.

Satir, P., Guerra, C., and Bell, A.J. (2007). Evolution and persistence of the cilium. Cell Motil. Cytoskeleton *64*, 906–913.

Sheth, R., Marcon, L., Bastida, M.F., Junco, M., Quintana, L., Dahn, R., Kmita, M., Sharpe, J., and Ros, M.A. (2012). Hox genes regulate digit patterning by controlling the wavelength of a Turing-type mechanism. Science *338*, 1476–1480.

Smith, H.L., Li, W., and Cheetham, M.E. (2015). Molecular chaperones and neuronal proteostasis. Semin. Cell Dev. Biol. *40*, 142–152.

Smith, U.M., Consugar, M., Tee, L.J., McKee, B.M., Maina, E.N., Whelan, S., Morgan, N.V., Goranson, E., Gissen, P., Lilliquist, S., et al. (2006). The transmembrane protein meckelin (MKS3) is mutated in Meckel-Gruber syndrome and the wpk rat. Nat. Genet. *38*, 191–196.

Stoetzel, C., Laurier, V., Davis, E.E., Muller, J., Rix, S., Badano, J.L., Leitch, C.C., Salem, N., Chouery, E., Corbani, S., et al. (2006). BBS10 encodes a vertebrate-specific chaperonin-like protein and is a major BBS locus. Nat. Genet. *38*, 521–524.

Tan, F.E., Vladar, E.K., Ma, L., Fuentealba, L.C., Hoh, R., Espinoza, F.H., Axelrod, J.D., Alvarez-Buylla, A., Stearns, T., Kintner, C., et al. (2013). Myb promotes centriole amplification and later steps of the multiciliogenesis program. Development *140*, 4277–4286.

Thornell, E., and Aquilina, A. (2015). Regulation of αA- and αB-crystallins via phosphorylation in cellular homeostasis. Cell. Mol. Life Sci. *72*, 4127–4137.

Tzekov, R., Stein, L., and Kaushal, S. (2011). Protein misfolding and retinal degeneration. Cold Spring Harb. Perspect. Biol. *3*, a007492.

Vertii, A., Bright, A., Delaval, B., Hehnly, H., and Doxsey, S. (2015). New frontiers: discovering cilia-independent functions of cilia proteins. EMBO Rep. *16*, 1275–1287.

Wheway, G., Abdelhamed, Z., Natarajan, S., Toomes, C., Inglehearn, C., and Johnson, C.A. (2013). Aberrant Wnt signalling and cellular over-proliferation in a novel mouse model of Meckel-Gruber syndrome. Dev. Biol. *377*, 55–66.

Wheway, G., Nazlamova, L., and Hancock, J.T. (2018). Signaling through the primary cilium. Front. Cell Dev. Biol. *6*, 1–13.

Wu, W., Huang, R., Wu, Q., Li, P., Chen, J., Li, B., and Liu, H. (2014). The role of Six1 in the genesis of muscle cell and skeletal muscle development. Int. J. Biol. Sci. *10*, 983–989.

Young, R.W. (1968). Passage of newly formed protein through the connecting cilium of retina rods in the frog. J. Ultrastruct. Res. *23*, 462–473.

Yuan, S., and Sun, Z. (2013). Expanding horizons: ciliary proteins reach beyond cilia. Annu. Rev. Genet. *47*, 353–376.

Zacharias, A.L., Lewandoski, M., Rudnicki, M.A., and Gage, P.J. (2011). Pitx2 is an upstream activator of extraocular myogenesis and survival. Dev. Biol. *349*, 395–405.

Zhou, S., Flamier, A., Abdouh, M., Tétreault, N., Barabino, A., Wadhwa, S., and Bernier, G. (2015). Differentiation of human embryonic stem cells into cone photoreceptors through simultaneous inhibition of BMP, TGFβ and Wnt signaling. Development *142*, 3294–3306.